

Optimization of the degenerate optical parametric oscillations threshold in bichromatically pumped microresonator

Nadezhda S. Tatarinova,^{1,2} Georgy V. Grechko,² Artem E. Shitikov,¹ Anatoly V. Masalov,^{1,3}
Igor A. Bilenko,^{1,4} Dmitry A. Chermoshentsev,^{1,2,*} and Valery E. Lobanov^{1,†}

¹*Russian Quantum Center, Skolkovo, Moscow 143025, Russia*

²*Moscow Institute of Physics and Technology, Dolgoprudny, Moscow Region 141700, Russia*

³*Lebedev Physical Institute, Russian Academy of Sciences, 119991 Moscow, Russia*

⁴*Faculty of Physics, Lomonosov Moscow State University, 119991 Moscow, Russia*

(Dated: April 15, 2025)

Integrated microring resonators have a broad range of applications in diverse fields with the potential to design compact, robust, energy efficient devices crucial for quantum applications. Degenerate optical parametric oscillations (DOPOs) realized in dual-pumped microring resonator (MRRs) with third-order optical nonlinearity are of special interest. They demonstrate both bistability of the phase of the excited signal mode and generation of non-classical light, that can be used for coherent photonic computing. Using coupled-mode equations we perform a comprehensive numerical analysis of DOPO conditions at normal group velocity dispersion (GVD) and bichromatic pump. Through both analytical and numerical approaches, we identify optimal setup parameters that minimize threshold power, highlighting the importance of considering the full spectrum of mode interactions. Additionally, we show that dispersion engineering, achievable in photonic molecules or photonic crystal microresonators, may provide a targeted frequency shift of specific microresonator modes resulting in pump power threshold reduction.

Keywords: integrated photonics, nonlinear optics, quantum optics, optical parametric oscillations

I. INTRODUCTION

Integrated photonic devices provide on-chip, robust, and scalable solutions for a wide range of applications, spanning from fundamental science to industrial technologies [1–6]. These applications include laser physics, spectroscopy, metrology, microwave photonics, quantum computing, communications, and sensing [7–15]. Advancements in fabrication techniques have enabled the production of CMOS-compatible, on-chip integrated waveguides and microring resonators (MRRs) with low optical loss and precise dispersion control, making them highly suitable for realizing efficient nonlinear and quantum optical interactions [16–19]. These developments have laid the foundation for a new generation of compact MRR-based devices, such as frequency comb generators [20, 21], microwave generators [22, 23], ultrastable lasers [24, 25], sources of non-classical states of light [26–28], and random number generators [29].

Among the nonlinear effects in microresonators, the excitation of degenerate optical parametric oscillations (DOPO) is of particular interest due to its applications in coherent computing, quantum computing, and random number generation [29–32]. Experimental realizations of DOPO have been demonstrated in media exhibiting either second-order $\chi^{(2)}$ or third-order $\chi^{(3)}$ nonlinearities [33–37].

One of the techniques for DOPO realization in MRRs with $\chi^{(3)}$ nonlinearity is based on the degenerate four-

wave mixing process and involves bichromatic (or dual) pumping of the microresonator modes [38]. Both theoretical and experimental studies have shown that MRRs with normal group velocity dispersion (GVD) are best suited for DOPO realization in dual-pumped setups [39]. The generated signal exhibits bistability between two phase states shifted by π , a crucial feature for implementing all-optical coherent Ising machines based on photonic integrated circuits [37, 40–42]. Furthermore, below the DOPO pump power threshold, the MRR can function as a generator of squeezed states of light [43]. However, fine-tuning of MRR properties, which could further optimize DOPO performance, remains an open area of research.

It is known that dispersion engineering significantly affects nonlinear processes in microresonators. Namely, the selective shifting of mode eigenfrequencies can enhance or suppress certain nonlinear processes, including parametric oscillation, the generation of frequency combs, and dissipative solitons [44–49]. Though the width and height of the waveguide are the main fabrication parameters that determine the dispersion profile in integrated microresonators, they are not the only factors [50–53]. For instance, a prominent dispersion engineering technique exploits avoided mode crossings in coupled resonator systems, also known as photonic molecules [48, 54, 55]. Another approach involves periodically varying the ring width, which alters the effective refractive index, forming a photonic crystal structure and leading to targeted mode splitting [56–59]. Such structures offer intriguing possibilities for compact chip-based devices [45, 46, 58–67]. We also applied targeted mode shifting to investigate its influence on the DOPO threshold. A comprehensive study on key parameters, including the second and higher

* d.chermoshentsev@gmail.com

† vallobanov@gmail.com

orders dispersion, frequency interval between the pumps, and their impact on the efficiency of dual-pumped MRR-based DOPOs, is still missing.

In this work, we theoretically investigate how parameters of the MRR with Kerr nonlinearity and the dual pumps affect the parametric threshold power and explore the methods to decrease it. We start with a simplified three-mode model, which reveals a minimum in the DOPO threshold in terms of pump power. Next, we perform a numerical study using a multimode model, in which we systematically analyze the dependence of the threshold pump power on the modeled system's parameters. While the optimal parameters are also found, they differ significantly from those of the three-mode model due to the influence of additional nonlinear frequency conversion processes. Finally, we numerically demonstrate that controlled dispersion engineering — specifically, a shift of the signal mode and a symmetrical shift of the particular sidebands — can substantially reduce the DOPO generation threshold. This approach paves the way for the new generation of energy-efficient optical sources for different quantum applications.

II. METHODS

A. Coupled mode equations

To model field dynamics inside the MRR with the bichromatic pumping, we use a set of normalized coupled mode equations (CMEs) [16, 68]:

$$\frac{\partial a_\mu}{\partial \tau} = -[1 - i\zeta_\mu] a_\mu + \delta_{+n,\mu} f_{+n} + \delta_{-n,\mu} f_{-n} + i \sum_{\mu' \leq \mu''} (2 - \delta_{\mu'\mu''}) a_{\mu'} a_{\mu''} a_{\mu'+\mu''-\mu}^* \quad (1)$$

Here a_μ is the normalized complex amplitude of the μ -th mode corresponding to the cold MRR frequency ω_μ , with relative eigenmode number μ . The dispersion of the cold MRR resonant frequencies is described by:

$$\omega_\mu = \omega_0 + D_1\mu + \frac{1}{2}D_2\mu^2 + \frac{1}{6}D_3\mu^3 + \dots, \quad (2)$$

where $D_1/2\pi$ is the MRR's free spectral range (FSR), $D_2/2\pi$ is the second-order dispersion coefficient and $D_3/2\pi$ is the third-order dispersion coefficient. The case $\mu = 0$ corresponds to the mode ω_0 , which is nearest to the arithmetic mean of the pump frequencies $\omega_{p\pm}$. $\tau = \kappa t/2$ denotes the normalized slow time, where κ is the cavity decay rate, consisting of both internal and coupling losses; $\delta_{\mu'\mu''}$ is the Kronecker delta. The normalized pump amplitudes are given by $f_{\pm n} = \sqrt{\frac{8\eta\hbar\omega_0^2cn_2}{\kappa^2n_0^2V_{\text{eff}}}} \sqrt{\frac{P_{\text{in},\pm}}{\hbar\omega_0}}$, where $\pm n$ is the relative eigenmode number of the MRR closest to the corresponding pump frequency, η is the ratio of coupling losses to the total cavity decay rate, $P_{\text{in},\pm}$ are the input pump powers, n_0 is the refractive index,

n_2 is the nonlinear refractive index, V_{eff} is the effective mode volume, c is the speed of light in vacuum, \hbar is the reduced Planck constant.

The terms ζ_μ represent the normalized frequency detunings from the MRR's equidistant frequency grid:

$$\zeta_\mu = \frac{\zeta_{+n} + \zeta_{-n}}{2} + \frac{\zeta_{+n} - \zeta_{-n}}{2n}\mu + \frac{d_2}{2}(n^2 - \mu^2), \quad (3)$$

with the normalized pump frequency detunings $\zeta_{\pm n} = 2(\omega_{p\pm} - \omega_{\pm n})/\kappa$ and $d_2 = 2D_2/\kappa$ is the normalized second-order dispersion coefficient. We limit the dispersion law to the second-order approximation for primary study. More details regarding normalization of these equations can be found in Appendix A.

From Eq. (1) and Eq. (3) it is evident that the system dynamics is fully characterized by the normalized pump parameters $(\pm n, f_{\pm n}, \zeta_{\pm n})$ and a single normalized MRR parameter (d_2). Our objective is to determine the optimal parameters of the dual-pumped MRR system for DOPO realization, focusing on minimizing power consumption, while ensuring that the signal mode a_0 is excited. Since we are analyzing a dual-pumped system, the total pump power $|f_{+n}|^2 + |f_{-n}|^2$ is chosen as one of the parameters for optimization.

B. Analytical three-mode model

We initiate our analysis with a simplified scenario involving only three interacting modes: two pumped modes with indices $\pm n$ (denoted as a_{+n} and a_{-n} for modes $+n$ and $-n$, correspondingly) and the signal (central) mode a_0 with index $\mu = 0$. For the near-the-threshold regime, we assume $|a_0|^2 \ll |a_{\pm n}|^2$.

The dynamics of the pumped modes can be described by the following equations:

$$\frac{\partial a_{\pm n}}{\partial \tau} = -[1 - i\zeta_{\pm n}] a_{\pm n} + i(|a_{\pm n}|^2 + 2|a_{\mp n}|^2) a_{\pm n} + f_{\pm n}. \quad (4)$$

Assuming a steady-state solution ($\partial a_{\pm n}/\partial \tau = 0$) for mode amplitudes $a_{\pm n}$ we obtain:

$$\frac{|f_{\pm n}|^2}{|a_{\pm n}|^2} = 1 + (\zeta_{\pm n} + |a_{\pm n}|^2 + 2|a_{\mp n}|^2)^2, \quad (5)$$

and the minimal total pump power is achieved with detunings

$$\zeta_{\pm n} = -|a_{\pm n}|^2 - 2|a_{\mp n}|^2, \quad (6)$$

and equals to

$$|f_{+n}|^2 + |f_{-n}|^2 = |a_{+n}|^2 + |a_{-n}|^2. \quad (7)$$

So, minimizing total pump power is equivalent to minimizing $|a_{+n}|^2 + |a_{-n}|^2$.

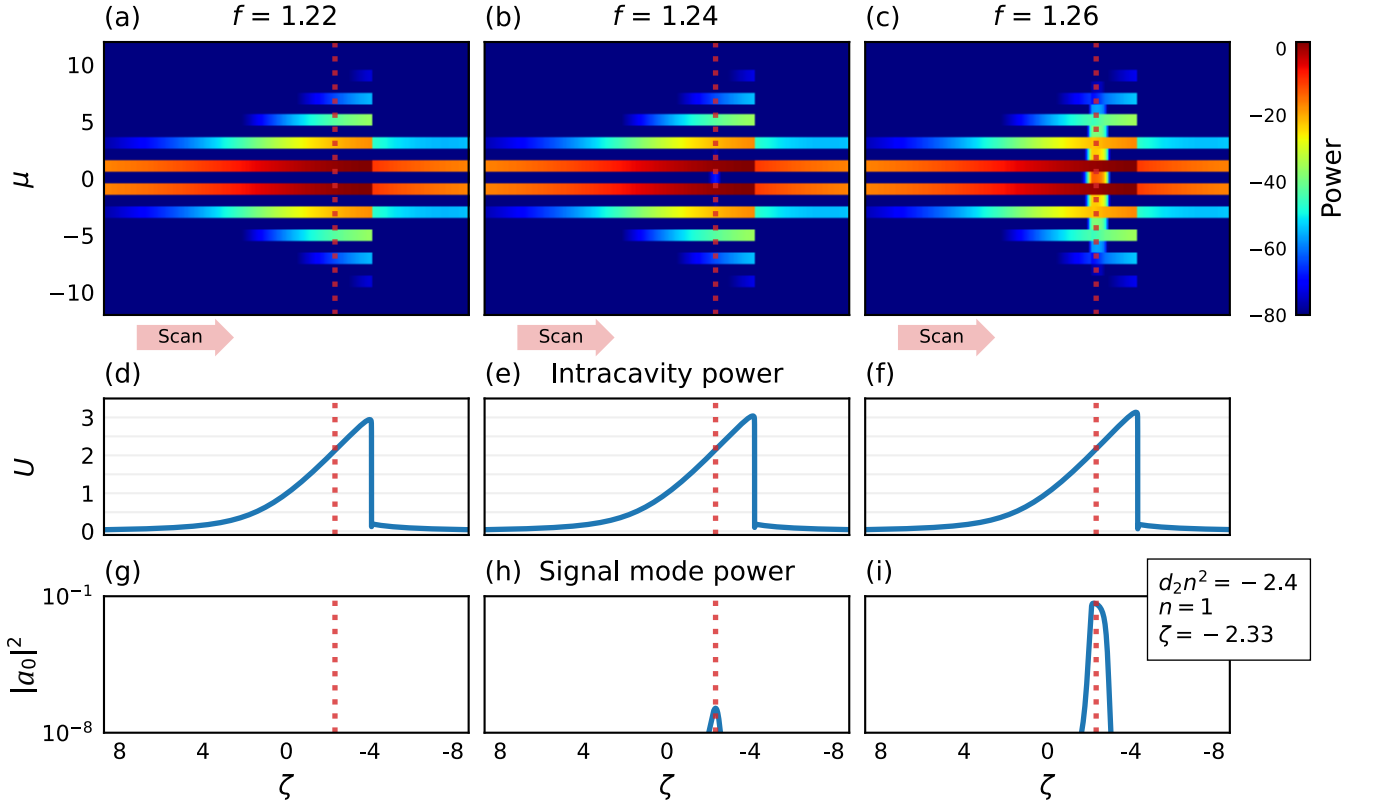


Figure 1. Intracavity power spectra for different pump amplitude values f with $d_2 n^2 = -2.4$ and $n = 1$. (a-c) Spectrograms for different pump regimes: power below the threshold (a), at the threshold (b), and above the threshold (c). Colorbar indicates spectrum components' relative power in a logarithmic scale: $10 \lg |a_\mu|^2$. (d-f) Intracavity power $U = \sum_\mu |a_\mu|^2$ in all regimes, respectively. (g-i) Signal mode power $|a_0|^2$ in all regimes, respectively. Red dashed lines denote the detuning $\zeta = -2.33$ corresponding to the generation of the signal mode a_0 , $\mu = 0$ in the threshold regime (h). All quantities are plotted in dimensionless units.

Equation for the signal mode is given by:

$$\frac{\partial a_0}{\partial \tau} = -[1 - i\zeta_0] a_0 + i(2|a_{+n}|^2 + 2|a_{-n}|^2) a_0 + 2ia_{+n}a_{-n}a_0^*, \quad (8)$$

where

$$\begin{aligned} \zeta_0 &= \frac{\zeta_{+n} + \zeta_{-n}}{2} + \frac{d_2}{2} n^2 = \\ &= -\frac{3}{2} (|a_{+n}|^2 + |a_{-n}|^2) + \frac{d_2}{2} n^2. \end{aligned} \quad (9)$$

This equation can be divided into separate equations for real and imaginary parts of a_0 (see Ref. [37]). The eigenvalues of the coefficient matrix for this system are:

$$\lambda_{1,2} = -1 \pm \sqrt{4|a_{+n}a_{-n}|^2 - [\zeta_0 + 2(|a_{+n}|^2 + |a_{-n}|^2)]^2}. \quad (10)$$

The signal mode can be excited only if $\text{Re } \lambda > 0$. At the threshold, where $\lambda = 0$, the following relationship is obtained:

$$\sqrt{4|a_{+n} + a_{-n}|^2 - \frac{1}{4}[d_2 n^2 + (|a_{+n}|^2 + |a_{-n}|^2)]^2} = 1. \quad (11)$$

By solving this equation for $|a_{-}|^2$ and subsequently minimizing the function $|a_{+}|^2 + |a_{-}|^2$, it can be determined that the minimum is achieved under the equal mode amplitude condition $|a_{+n}|^2 = |a_{-n}|^2$, which leads [from Eq. (6)] to the necessary condition of equal detunings $\zeta_{+n} = \zeta_{-n}$ and pump powers $|f_{+n}|^2 = |f_{-n}|^2$. The simplest way to satisfy these conditions is to use the symmetric frequency scan. Taking this into consideration, we also derive the threshold power of each pump $f_{\text{thr}} = |f_{+n}| = |f_{-n}|$:

$$|f_{\text{thr}}|^2 = \frac{1}{6} \left(d_2 n^2 + 2\sqrt{3 + (d_2 n^2)^2} \right). \quad (12)$$

This expression indicates that the threshold power depends on $d_2 n^2$ parameter. The minimum is reached for $d_2 n^2 = -1$, indicating that normal GVD is required.

From this simplified three-mode model, we obtain analytically the optimal parameters of the MRR and pumps that minimize the input pumping power

$$|f_{+n}|^2 = |f_{-n}|^2 = \frac{1}{2}, \quad \zeta_{+n} = \zeta_{-n} = -\frac{3}{2}, \quad d_2 n^2 = -1. \quad (13)$$

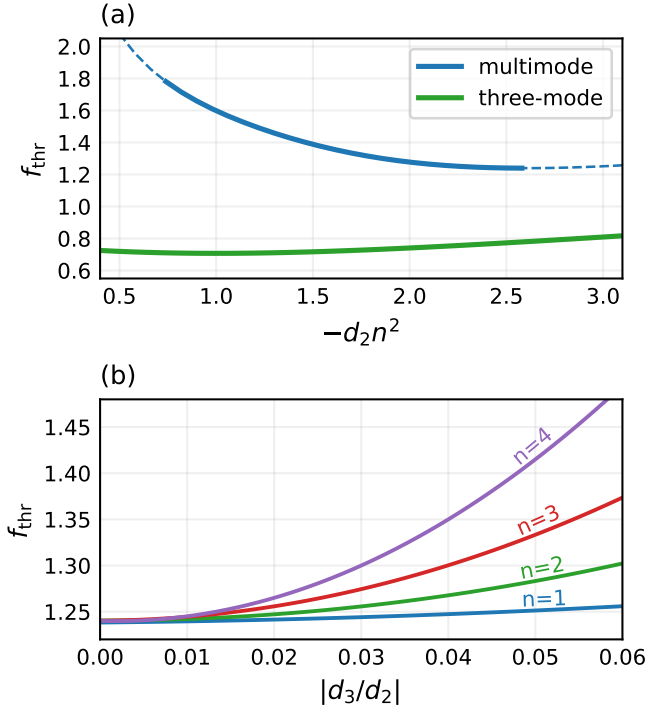


Figure 2. (a) Threshold amplitude f_{thr} dependence on the dispersion parameter $-d_2 n^2$ for the analytical solution of the three-mode model (green line) and the numerical solution of the multimode model (blue line). The dashed line shows the areas where the other modes between the pumps in case of $n > 1$ are already excited. (b) Threshold amplitude as a function of the added third-order dispersion for a fixed $d_2 n^2 = -2.6$ parameter for different numbers of pumped modes. All quantities are plotted in dimensionless units.

C. Numerical simulation

The examined three-mode model does not account for additional nonlinear processes of the multimode interaction present in real-life scenarios, requiring additional analysis [69]. Therefore, we numerically solve a system of 256 CMEs for the dual-pumped MRR [Eq. (1)] using Fast Fourier Transform methods for nonlinear terms calculation [70]. We verified that a further increase in the number of CMEs does not change the results. The CME approach allows us to observe the dynamics of individual modes directly. We use a symmetrical linear frequency scan ($\zeta = \zeta_{+n} = \zeta_{-n}, f = f_{+n} = f_{-n}$), moving from the blue-detuned region to the red-detuned by progressively decreasing ζ , for different d_2, n, f parameters. The higher-order dispersion coefficients are neglected. To account for vacuum fluctuations in this system, we initialize each eigenmode of the MRR with a noise-like seed input having a mean amplitude of 10^{-4} at every step of the simulation.

The threshold power is determined by monitoring the intracavity power of the signal mode and identifying the point at which it exceeds the initial noise level. Notably,

reducing the scan rate does not influence the threshold. The simulation results for different pump powers and $d_2 n^2 = -2.4$ are presented in Fig. 1. For f below the threshold, only the non-degenerate processes occur, forming a few teeth of the primary comb with $2n \times \text{FSR}$ spacing [Fig. 1(a)]. In the threshold regime, the signal mode $\mu = 0$ is generated at the particular detuning $\zeta = -2.33$ [Fig. 1(h)]. For the further increasing pump power, the signal mode power is increasing and the lines between primary comb teeth start generating [Fig. 1(c)]. Moreover, we verified that the proposed threshold condition accurately identifies the point at which parametric oscillations occur. We observe the quadrature-squeezed vacuum if the pump power is below the threshold, and phase-bistable signal if the power exceeds this threshold (see Appendix B).

The threshold power values found for the wide range of dispersion parameters are presented in Fig. 2(a). The green line corresponds to the analytical three-mode model, and the blue line is the multimode approach results. The threshold power value shows a significant increase from its analytical counterpart, with the new minimal pump amplitude $f_{\text{thr}} = 1.24$ corresponding to a dispersion parameter near $d_2 n^2 = -2.6$. It is noteworthy that, similar to the three-mode model, the threshold power remains independent of the indices of pumped modes when the $-d_2 n^2$ parameter is fixed. The dashed areas along the blue line correspond to the threshold of the parametric signal for $n = 1$. For the case $n > 1$ other modes between the pumps are already excited prior to the signal one. Fig. 3 shows the spectrograms and intracavity spectra at the detuning $\zeta = -2.33$, corresponding to central mode generation, at different values of $d_2 n^2$ and with the 6-FSR interval between pumps. One may see that with the increasing of $|d_2|n^2$ for the fixed pump amplitude $f = 1.24$ the power of the modes with indices $\mu = \pm 1$ becomes pronounced instead of the signal mode $\mu = 0$. One may take into account this fact in the experiment.

From the numerical study of the multimode model we obtain optimal parameters of the pump and microresonator $|f_{\text{thr}}| = 1.24$, $d_2 n^2 = -2.6$ that differ significantly from the analytical ones in Eq. (13) due to the nonlinear interactions between all modes of the MRR. At low $|d_2|n^2 < 0.7$ the threshold power rapidly increases. The value of $d_2 n^2$ determines the relatively high value of the frequency interval between pumps n , since d_2 value is usually of order of magnitude $10^{-1} - 10^{-2}$. On the other hand, with the higher n the influence of the higher order dispersion becomes more pronounced.

To study the influence of the high-order dispersion on the threshold power values, we extend the normalized dispersion equation derived from Eq. (3):

$$\zeta_{\mu}^{\text{third order}} = \zeta_{\mu} + \frac{d_3}{6} (n^3 - \mu^3), \quad (14)$$

where $d_3 = 2D_3/\kappa$ is the normalized third-order dispersion coefficient. In our modeling, we introduce a small

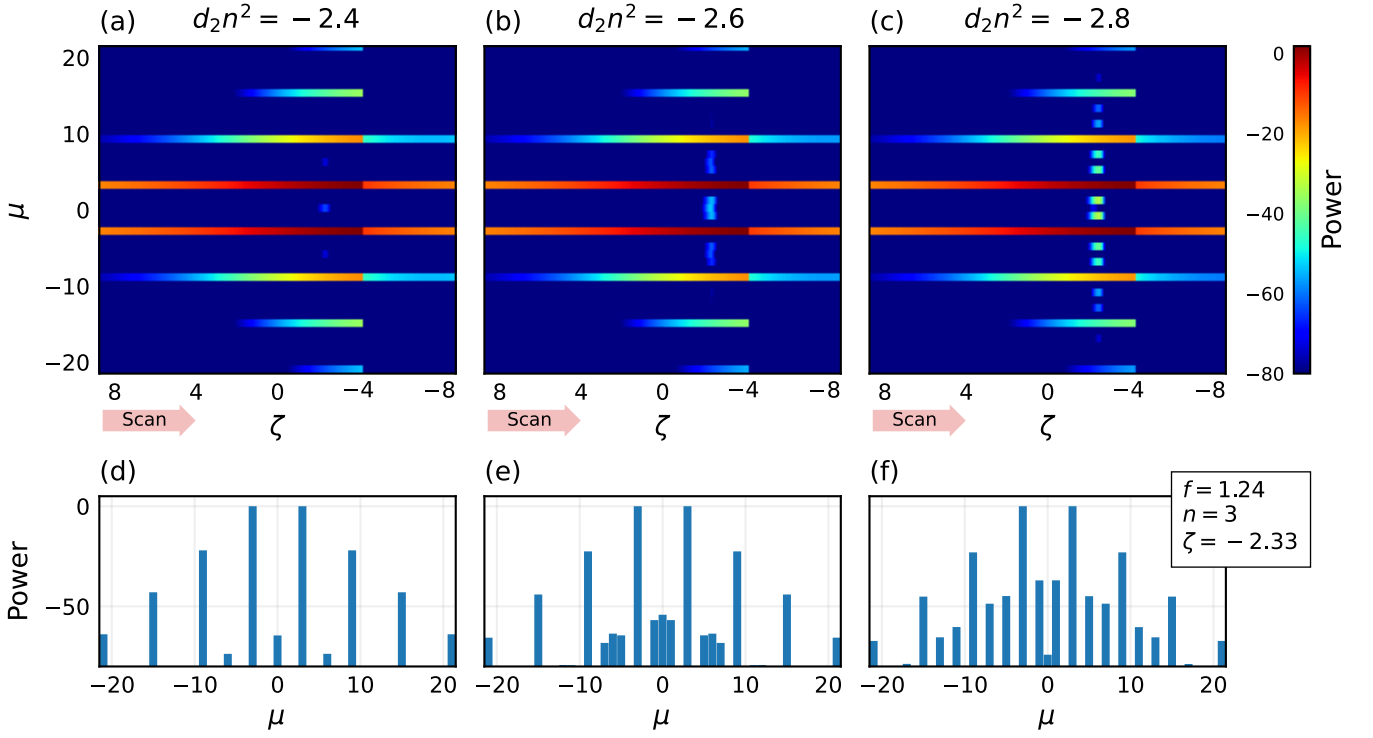


Figure 3. Spectrograms (a-c) and spectra for pumps detuning $\zeta = -2.33$ (d-f) for different dispersion values for fixed near-threshold pump amplitude $f = 1.24$. For lower absolute dispersion the signal mode starts generating earlier (a, d), for higher absolute dispersion values the adjacent modes appear earlier despite the generation of the signal mode (c, f). In all cases the signal mode $\mu = 0$ is excited. Threshold values were calculated for $n = 3$. All quantities are plotted in dimensionless units.

deviation from the second-order approximation using the ratio $|d_3/d_2|$ with the parameter $d_2n^2 = -2.6$ fixed. The outcome shows that increasing n results in a rapid increase of the threshold power [Fig. 2(b)]. However, up to $|d_3/d_2| < 0.01$ the threshold weakly depends on n and for the further study we assume $d_3 = 0$.

D. Performance enhancement via dispersion engineering

Innovative fabrication techniques provide an opportunity to manipulate the dispersion law of MRR precisely. One of the methods proved to enhance nonlinear processes is the targeted mode shifting [48, 71–74], which can be experimentally realized using photonic molecules [44, 75, 76] or photonic crystals [45, 49, 63, 77]. We implement this method for our investigation of the optimal parameters.

Numerically, it can be described by introducing a frequency shift Δ_ν of the resonator eigenmodes ν . The expression for the frequency of the μ -th mode is:

$$\omega_\mu = \omega_0 + \delta_{\mu\nu}\Delta_\nu + D_1\mu + \frac{1}{2}D_2\mu^2. \quad (15)$$

First, we introduce the frequency shift into the central mode $\nu = 0$. The modified normalized detuning for the

central mode, which is introduced in the CMEs, differs from Eq. (3): $\zeta_0^{\text{shift}} = \zeta_0 - 2\Delta_0/\kappa$. In Fig. 4(a) the dependence of the DOPO threshold on the mode frequency shift for several values d_2n^2 is presented. All the curves are calculated for reasonable $n = 5$. We verified that changing n and d_2 accordingly to maintain the parameter d_2n^2 fixed does not affect the threshold power.

It is found that introducing a negative shift $\Delta_0 < 0$ of the central mode can significantly reduce the threshold pump power. For each dispersion parameter, there exists an optimal shift value that provides the minimal threshold. For $d_2n^2 = -1.0$, the minimum is not pronounced within the range of selected shift values ($|\Delta_0| < 1.2$), and the threshold pump amplitude f_{thr} remains well above 1.0. As $|d_2|n^2$ increases, a clear and wide minimum appears. The minimum value decreases with increasing $|d_2|n^2$ and drifts to the larger absolute value of Δ_0 . For example, we obtained a minimum $f_{\text{thr}} = 0.835$ for $d_2n^2 = -5.0$, which is more than 50% lower than for the microring without mode shifting.

The threshold is calculated over a wide range of parameters d_2n^2 and Δ_0 . The results are presented in Fig. 4(b). The white area in the colormap corresponds to the appearance of the non-central modes prior to the DOPO signal. The presence of the excited modes between pumps may decrease the level of squeezing of the output parametric signal. It is worth noting that in the area of low

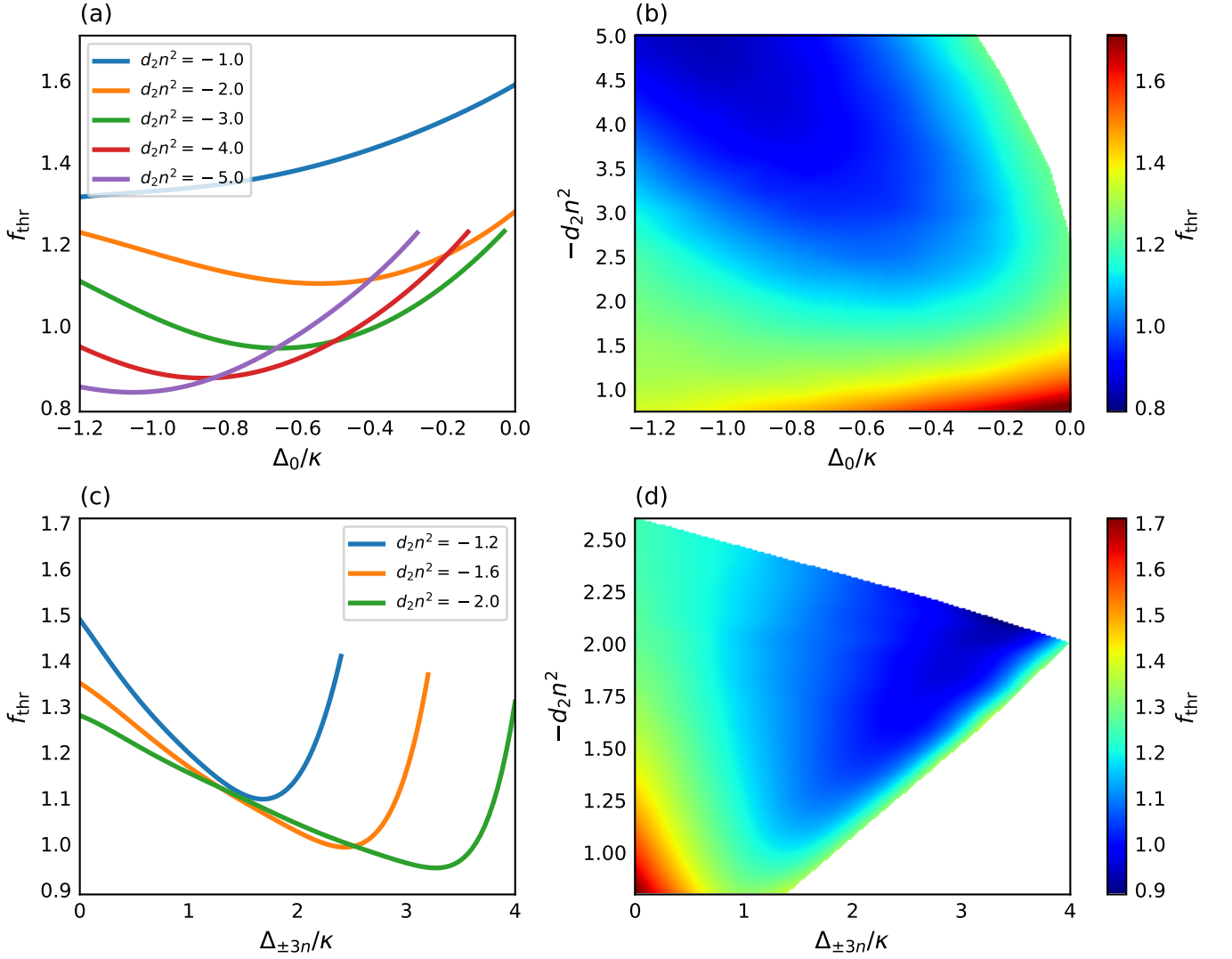


Figure 4. (a) The dependence of the DOPO threshold on the signal mode $\nu = 0$ normalized frequency shift. The lines correspond to the dependence for a different fixed $d_2 n^2$. (b) Colormap for the threshold pump amplitude f_{thr} vs normalized shift of the central frequency Δ_0 and the dispersion parameter $-n^2 d_2$. The minimum $f = 0.835$ is observed at $\Delta_0 = -1.125\kappa$ and $d_2 n^2 = -5.0$. White areas correspond to the existence of the modes between pumped ones prior to the generation of the signal mode. Threshold values were calculated for $n = 5$. (c) The dependence of the DOPO threshold on the simultaneous modes $\nu = \pm 3n$ frequency shift ($\Delta_{+3n} = \Delta_{-3n}$). The lines correspond to the dependence for a different fixed $d_2 n^2$. (d) Colormap for the threshold pump amplitude f_{thr} vs normalized shift of the sideband frequencies (with relative indices $3n$ and $-3n$) $\Delta_{\pm 3n}$ and the dispersion parameter $d_2 n^2$. The minimum $f = 0.95$ is observed at $\Delta_{\pm 3n} = 3.4\kappa$ and $d_2 n^2 = -2.0$. White area corresponds to the existence of the modes between pumped ones prior to the generation of the signal mode. Threshold values were calculated for $n = 3$. All quantities are plotted in dimensionless units.

frequency shift ($|\Delta_0|/\kappa < 0.2$) the threshold pump amplitude is relatively high ($f_{\text{thr}} > 1.0$) for any $d_2 n^2$.

We also study the effects of the symmetrical shifting of the modes $\nu = \pm 3n$. Such structures are experimentally feasible and are investigated for frequency comb generation in [77]. The detunings in the model in this case are $\zeta_{+3n}^{\text{shift}} = \zeta_{+3n} - 2\Delta_{+3n}/\kappa$ and $\zeta_{-3n}^{\text{shift}} = \zeta_{-3n} - 2\Delta_{-3n}/\kappa$. It is shown in Fig. 4(c) that for the fixed dispersion parameter the threshold power slowly decreases with increasing absolute shift value until the minimum for the given dispersion is reached; then we observe an abrupt increase in

threshold power. In this case, the threshold power is decreased to $f = 0.95$. We also limit the parameter region to the values that allow observation of the signal mode without excited adjacent components. A colormap for the wide range of parameters is shown in Fig. 4(d). We confirmed that keeping $d_2 n^2$ constant by adjusting n and d_2 does not affect the threshold power.

The mechanism underlying this threshold power decrease is illustrated in Fig. 5: the shift of the sidebands results in the higher energy conversion to other MRR's modes from the pumping. Thus, the parametric signal

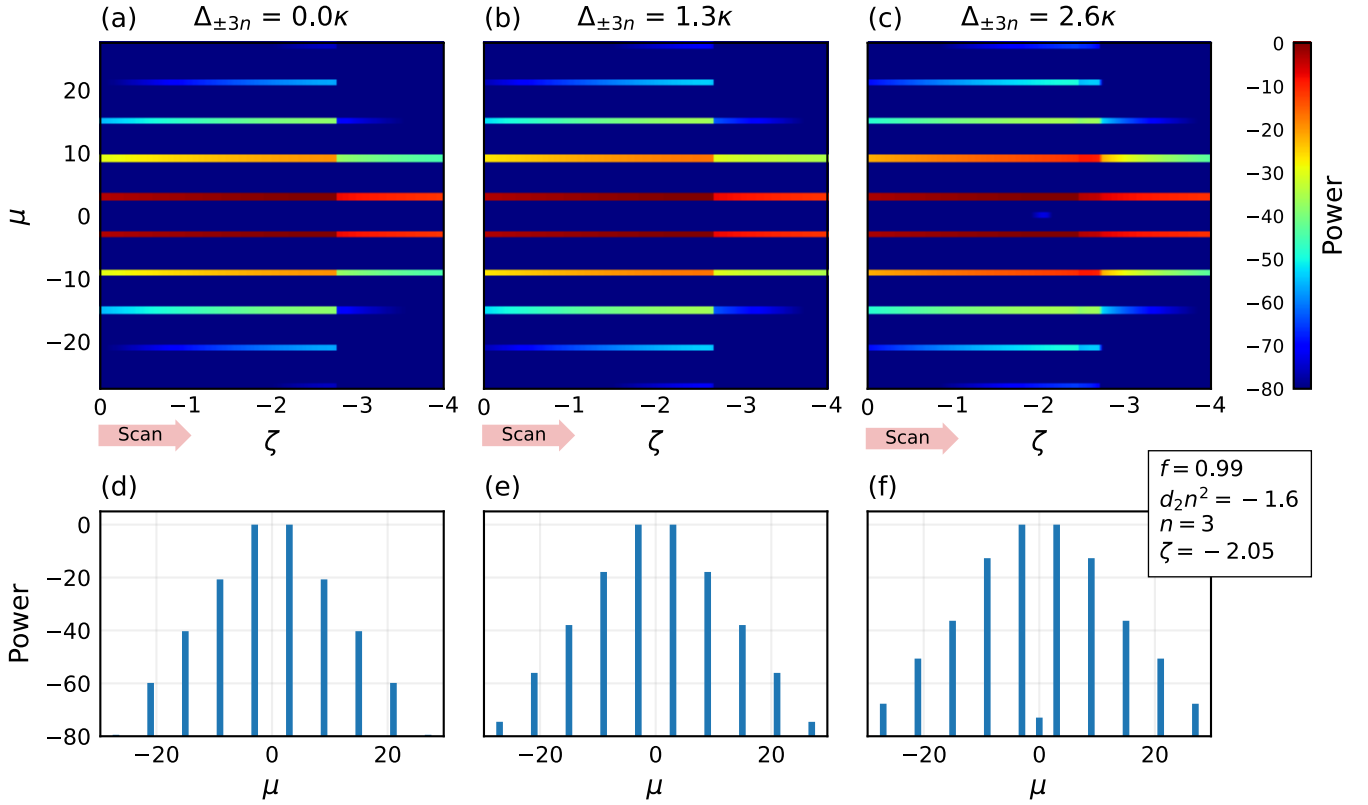


Figure 5. Spectrograms (a-c) for different shift values of the $\pm 3n$ -th modes for fixed pump amplitude $f = 0.99$ and dispersion coefficient $d_2 n^2 = -1.6$ and $n = 3$. The indices of the shifted modes are $\nu = \pm 3n = \pm 9$. The energy conversion efficiency from the pumps to the sidebands is increasing with the increment of the shift $\Delta_{\pm 3n}$ (d-f) as shown for the detuning $\zeta = -2.05$ corresponding to the generation of the signal mode (f). Primarily generated sidebands start to participate in the parametric signal generation, thus, lowering required input pumps power. All quantities are plotted in dimensionless units.

generation is enhanced via the participation of the secondary modes in the parametric process.

It is worth noting that the direction of the symmetrical shift of the sidebands $\pm 3n$ is different from the shift of the central mode. Also, the shift of the central mode is more effective for large $|d_2|n^2$ values, and it requires smaller absolute shift values compared to the shift of $\pm 3n$ modes.

We verified that the introduced targeted mode shifting does not perturb the bistability of the phase of the parametric signal. This is analyzed via the output signal mode amplitude realizations on the complex plane (described in Appendix B).

III. RESULTS AND DISCUSSION

We have analytically and numerically derived the threshold pump amplitudes for a DOPO realized in a symmetrically bichromatically pumped single MRR with $\chi^{(3)}$ nonlinearity and normal GVD. Using three-mode model approximation, we found the optimal parameters and showed analytically the requirement of equal detunings and powers of the pumps. Then we use the CMEs

to simulate the amplitudes evolution in the multimode approach.

The threshold parameters obtained from the full multimode model $f = 1.24$ differ significantly from those predicted by the approximate three-mode model $f = 1/\sqrt{2} \approx 0.7$, highlighting the importance of considering the full spectrum of mode interactions in the MRR for accurate predictions. Our analysis shows that the minimum of the DOPO pump power threshold occurs at different dispersion parameters in the two models: $d_2 n^2 = -1$ for the three-mode model and $d_2 n^2 = -2.6$ for the multimode model. Despite these differences, both models show an independence of the DOPO threshold value on the index n of the pumped modes when the product $d_2 n^2$ is fixed. Introducing higher-order dispersion approximation into the model reveals that the threshold power increases significantly with increasing frequency interval between the pumps.

We have shown that it is possible to reduce the threshold of the process by introducing shifts of certain modes, specifically, one central mode or two modes with indices $\pm 3n$. It has been shown that, for each dispersion parameter, there is an optimal value of the shift of the corresponding modes. Introducing a frequency shift of

-1.125κ in the signal mode at $d_2 n^2 = -5.0$, the threshold DOPO pump power can be reduced by more than 50%, achieving a minimum threshold pump amplitude of $f = 0.835$. That can be of special importance for energy efficiency enhancement of the developed devices and reducing the impact of the thermal effects [74].

Further research in this direction will help refine the models for practical applications in integrated photonic devices and pave the way for engineering compact (in future, chip-based) and energy-efficient “turn-key” devices. The results we have obtained offer valuable insights into the study and understanding of the four-wave mixing process in a microresonator with bichromatic pumping and advance the practical application of such techniques in the development of various photonic devices.

ACKNOWLEDGMENTS

The theoretical analysis was supported by Rosatom in the framework of the Roadmap for Quantum computing (Contract No. 868-1.3-15/15-2021 dated October 5).

The numerical simulations were supported by the Russian Science Foundation (Grant No. 23-42-00111).

N. S. T. developed the theory, with the assistance from G. V. G. and D. A. C.; N. S. T. and V. E. L. performed the simulations and analyzed the results, with the assistance from A. V. M.; N. S. T., V. E. L., A. E. S. and D. A. C. wrote the manuscript, with input from others; I. A. B., D. A. C. and V. E. L. supervised the project. All authors discussed the results and reviewed the manuscript.

The authors declare no competing interests.

DATA AVAILABILITY

The data that support the findings of this study are available from the authors upon reasonable request.

Appendix A: Coupled mode equations

The field dynamics inside the MRR can be described using the slow varying amplitude approximation at the signal resonance frequency ω_0 . The CMEs for the modes of the MRR are given by:

$$\begin{aligned} \frac{\partial A_\mu}{\partial t} = & -\frac{\kappa}{2} A_\mu + \delta_{+n\mu} \sqrt{\kappa_{\text{ext}} \frac{P_{\text{in},+n}}{\hbar\Omega_{+n}}} e^{-i(\Omega_{+n}-\omega_{+n})t} + \\ & \delta_{-n\mu} \sqrt{\kappa_{\text{ext}} \frac{P_{\text{in},-n}}{\hbar\Omega_{-n}}} e^{-i(\Omega_{-n}-\omega_{-n})t} + \\ & ig \sum_{\mu'\mu''\mu'''} A_{\mu'} A_{\mu''} A_{\mu'''}^* e^{i(\omega_{\mu'}+\omega_{\mu''}-\omega_{\mu'''}-\omega_\mu)t}, \end{aligned} \quad (\text{A1})$$

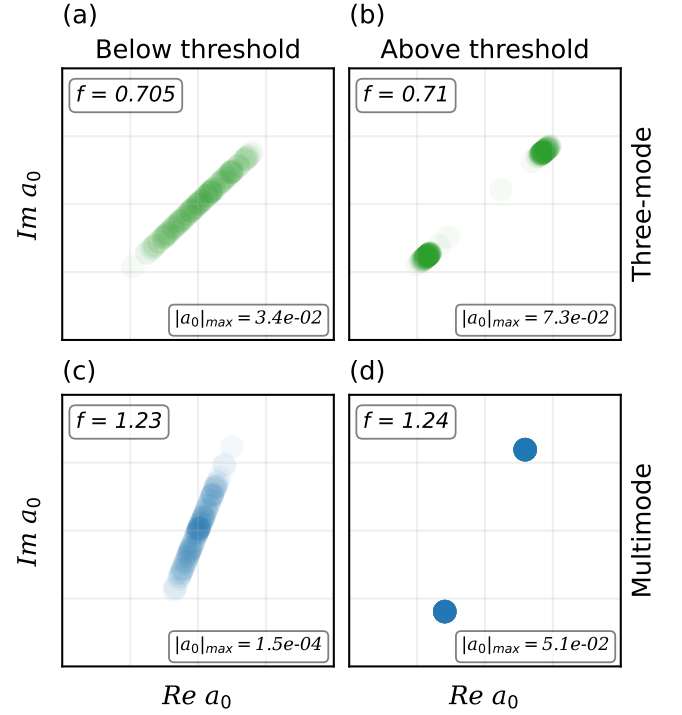


Figure 6. Realizations of complex amplitude of the signal mode a_0 for different regimes in the three-mode model with the optimal parameters $d_2 n^2 = -1.0$ (a,b) and in the multimode model with the optimal parameters $d_2 n^2 = -2.4$ (c,d). All quantities are plotted in dimensionless units.

where A_μ is the amplitude of the MRR’s eigenfrequency, normalized such that $|A_\mu|^2$ corresponds to the number of photons in that mode, κ_{ext} is the coupling rate and $\kappa = \kappa_{\text{int}} + \kappa_{\text{ext}}$ is the full resonator decay rate with κ_{int} denoting the intrinsic loss of the MRR. The nonlinear coupling coefficient g is given by:

$$g = \frac{\hbar\omega_0^2 cn_2}{n_0^2 V_{\text{eff}}}, \quad (\text{A2})$$

where n_0 is the refractive index, n_2 is the nonlinear refractive index, V_{eff} is the effective mode volume.

The pumps are introduced in Eq. (A1) via pump powers $P_{\text{in},\pm}$ and pump frequencies $\omega_{p\pm}$, which are detuned from the MRR’s eigenfrequencies $\omega_{\pm n}$, respectively.

We normalize these equations as follows:

$$a_\mu = \sqrt{\frac{2g}{\kappa}} A_\mu e^{-\left(\omega_\mu - \frac{\omega_{p+} + \omega_{p-}}{2} - \mu \frac{\omega_{p+} - \omega_{p-}}{2n}\right)t}, \quad (\text{A3})$$

where a_μ is the normalized mode amplitude. This normalization results in the time-independent terms and accounts for the phase shift due to deviations from an equidistant frequency grid. With bichromatic pumping, the effective FSR of the system is $(\omega_{p+} - \omega_{p-})/(2n)$.

From Eq. (A3) other values are normalized as follows: $\tau = t\kappa/2$ is the slow time, the pump amplitudes

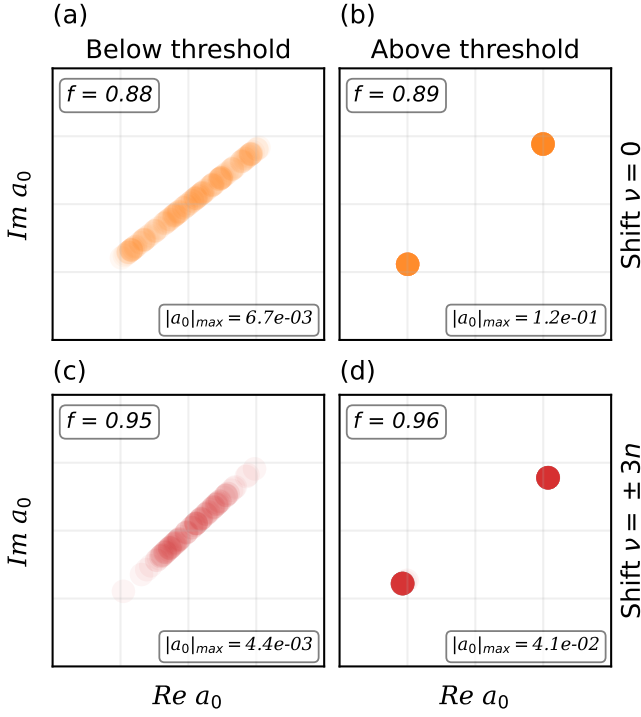


Figure 7. Realizations of complex amplitude of the signal mode a_0 for different regimes in the model with the shift of the central mode for parameters $d_2 n^2 = -4.0$ and $\Delta_0 = -0.75\kappa$ (a,b) and in the model with the shifts of the sidebands for parameters $d_2 n^2 = -2.0$ and $\Delta_{\pm 3n} = 3.4\kappa$ (c,d). All quantities are plotted in dimensionless units.

$f_{\pm n} = \sqrt{\frac{8\kappa_{\text{ext}}g}{\kappa^3}} \sqrt{\frac{P_{\text{in},\pm}}{\hbar\omega_0}}$. Formally, it is necessary to normalize the pump amplitudes by their respective frequencies; however, we assume that ω_0 and $\omega_{p\pm}$ are close enough that their difference can be neglected. The normalized second-order coefficient is given by $d_2 = 2D_2/\kappa$

and detuning [see Eq. (3)]:

$$\zeta_\mu = \frac{\zeta_{+n} + \zeta_{-n}}{2} + \frac{\zeta_{+n} - \zeta_{-n}}{2n}\mu + \frac{d_2}{2}(n^2 - \mu^2), \quad (\text{A4})$$

where $\zeta_{\pm n} = 2(\omega_{p\pm} - \omega_{\pm n})/\kappa$ denote the normalized pumps detunings from corresponding MRR eigenmode.

Appendix B: Squeezing

In dual-pumped systems operating below the DOPO threshold regime, a squeezed vacuum state is generated in the signal mode. If the pump power is above threshold, the signal field bifurcates to two possible states with phases offset by π . To verify the obtained threshold parameters, we perform numerical simulations of the experimental process, collecting statistical data from simulations with various initial vacuum noise seed fields.

Firstly, we examine both the three-mode and multi-mode models (see Fig. 6). In both models, the generated signal field exhibits quadrature squeezing for input powers below the threshold values. Over one hundred realizations at low tuning speed were made to calculate the data for each panel of Fig. 6. In the above threshold regime, following a non-equilibrium transition, the generated signal stabilizes in one of two possible states with a phase offset of π .

Secondly, we perform the same procedure using the models with shifts. The results (Fig. 7) coincide with the threshold definition.

It is important to note that these results reflect the squeezing *inside* the MRR. The output signal, however, will be affected due to coupling losses. As the theoretical results are expressed in normalized units, the threshold power value f_{thr} does not change, but the coupling is taken into account in its normalization, as detailed in Appendix A. Consequently, the output squeezing factor is highly dependent on the input power in real units. To achieve higher squeezing, it is necessary to increase the coupling coefficient and, hence, the input power.

[1] K. J. Vahala, Optical microcavities, *Nature* **424**, 839 (2003).
 [2] D. Marpaung, C. Roeloffzen, R. Heideman, A. Leinse, S. Sales, and J. Capmany, Integrated microwave photonics, *Laser & Photonics Reviews* **7**, 506 (2013).
 [3] H. Lin, Z. Luo, T. Gu, L. C. Kimerling, K. Wada, A. Agarwal, and J. Hu, Mid-infrared integrated photonics on silicon: a perspective, *Nanophotonics* **7**, 393 (2018).
 [4] P. Cheben, R. Halir, J. H. Schmid, H. A. Atwater, and D. R. Smith, Subwavelength integrated photonics, *Nature* **560**, 565 (2018).
 [5] D. Pérez, I. Gasulla, P. D. Mahapatra, and J. Capmany, Principles, fundamentals, and applications of programmable integrated photonics, *Adv. Opt. Photon.* **12**, 709 (2020).

[6] D. Zhu, L. Shao, M. Yu, R. Cheng, B. Desiatov, C. J. Xin, Y. Hu, J. Holzgrafe, S. Ghosh, A. Shams-Ansari, E. Puma, N. Sinclair, C. Reimer, M. Zhang, and M. Lončar, Integrated photonics on thin-film lithium niobate, *Adv. Opt. Photon.* **13**, 242 (2021).
 [7] A. Pasquazi, M. Peccianti, B. E. Little, S. T. Chu, D. J. Moss, and R. Morandotti, Stable, dual mode, high repetition rate mode-locked laser based on a microring resonator, *Opt. Express* **20**, 27355 (2012).
 [8] D. Liang, X. Huang, G. Kurczveil, M. Fiorentino, and R. G. Beausoleil, Integrated finely tunable microring laser on silicon, *Nature Photonics* **10**, 719 (2016).
 [9] C. Weimann, M. Lauermaun, F. Hoeller, W. Freude, and C. Koos, Silicon photonic integrated circuit for fast and precise dual-comb distance metrology, *Opt. Express* **25**,

- 30091 (2017).
- [10] P. Marin-Palomo, J. N. Kemal, M. Karpov, A. Kordts, J. Pfeifle, M. H. P. Pfeiffer, P. Trocha, S. Wolf, V. Brasch, M. H. Anderson, R. Rosenberger, K. Vijayan, W. Freude, T. J. Kippenberg, and C. Koos, Microresonator-based solitons for massively parallel coherent optical communications, *Nature* **546**, 274 (2017).
 - [11] K. D. Heylman, K. A. Knapper, E. H. Horak, M. T. Rea, S. K. Vanga, and R. H. Goldsmith, Optical microresonators for sensing and transduction: A materials perspective, *Advanced Materials* **29**, 1700037 (2017).
 - [12] Z. Yang, M. Jahanbozorgi, D. Jeong, S. Sun, O. Pfister, H. Lee, and X. Yi, A squeezed quantum microcomb on a chip, *Nature Communications* **12**, 4781 (2021).
 - [13] E. Pelucchi, G. Fagas, I. Aharonovich, D. Englund, E. Figueroa, Q. Gong, H. Hannes, J. Liu, C.-Y. Lu, N. Matsuda, J.-W. Pan, F. Schreck, F. Sciarrino, C. Silberhorn, J. Wang, and K. D. Jöns, The potential and global outlook of integrated photonics for quantum technologies, *Nature Reviews Physics* **4**, 194 (2022).
 - [14] Z. Zhang, S. Zhang, X. Liu, Z. Wei, T. Sharma, G. S. Murugan, H. K. Tsang, T. Liu, and Z. Cheng, Integrated optical spectrometers on silicon photonics platforms, *Laser & Photonics Reviews* **19**, 2400155 (2025).
 - [15] L. Labonté, O. Alibart, V. D'Auria, F. Doutre, J. Etesse, G. Sauder, A. Martin, E. Picholle, and S. Tanzilli, Integrated photonics for quantum communications and metrology, *PRX Quantum* **5**, 010101 (2024).
 - [16] T. Herr, K. Hartinger, J. Riemensberger, C. Y. Wang, E. Gavartin, R. Holzwarth, M. L. Gorodetsky, and T. J. Kippenberg, Universal formation dynamics and noise of Kerr-frequency combs in microresonators, *Nature Photonics* **6**, 480 (2012).
 - [17] T. Herr, V. Brasch, J. D. Jost, C. Y. Wang, N. M. Kondratiev, M. L. Gorodetsky, and T. J. Kippenberg, Temporal solitons in optical microresonators, *Nature Photonics* **8**, 145 (2014).
 - [18] D. V. Strekalov, C. Marquardt, A. B. Matsko, H. G. L. Schwefel, and G. Leuchs, Nonlinear and quantum optics with whispering gallery resonators, *Journal of Optics* **18**, 123002 (2016).
 - [19] T. J. Kippenberg, A. L. Gaeta, M. Lipson, and M. L. Gorodetsky, Dissipative Kerr solitons in optical microresonators, *Science* **361**, eaan8083 (2018).
 - [20] T. J. Kippenberg, R. Holzwarth, and S. A. Diddams, Microresonator-based optical frequency combs, *Science* **332**, 555 (2011).
 - [21] W. Wang, S. T. Chu, B. E. Little, A. Pasquazi, Y. Wang, L. Wang, W. Zhang, L. Wang, X. Hu, G. Wang, H. Hu, Y. Su, F. Li, Y. Liu, and W. Zhao, Dual-pump Kerr micro-cavity optical frequency comb with varying FSR spacing, *Scientific Reports* **6**, 28501 (2016).
 - [22] I. Kudelin, W. Groman, Q.-X. Ji, J. Guo, M. L. Kelleher, D. Lee, T. Nakamura, C. A. McLemore, P. Shirmohammadi, S. Hanifi, H. Cheng, N. Jin, L. Wu, S. Halladay, Y. Luo, Z. Dai, W. Jin, J. Bai, Y. Liu, W. Zhang, C. Xiang, L. Chang, V. Ilchenko, O. Miller, A. Matsko, S. M. Bowers, P. T. Rakich, J. C. Campbell, J. E. Bowers, K. J. Vahala, F. Quinlan, and S. A. Diddams, Photonic chip-based low-noise microwave oscillator, *Nature* **627**, 534 (2024).
 - [23] S. Li, K. Yu, D. A. Chermoshentsev, W. Sun, J. Long, X. Yan, C. Shen, A. E. Shitikov, N. Y. Dmitriev, I. A. Bilenko, and J. Liu, Universal Kerr-thermal dynamics of self-injection-locked microresonator dark pulses, arXiv:2502.03001.
 - [24] J. Guo, C. A. McLemore, C. Xiang, D. Lee, L. Wu, W. Jin, M. Kelleher, N. Jin, D. Mason, L. Chang, A. Feshali, M. Paniccia, P. T. Rakich, K. J. Vahala, S. A. Diddams, F. Quinlan, and J. E. Bowers, Chip-based laser with 1-hertz integrated linewidth, *Science Advances* **8**, eabp9006 (2022).
 - [25] N. M. Kondratiev, V. E. Lobanov, A. E. Shitikov, R. R. Galiev, D. A. Chermoshentsev, N. Y. Dmitriev, A. N. Danilin, E. A. Lonshakov, K. N. Min'kov, D. M. Sokol, S. J. Cordette, Y.-H. Luo, W. Liang, J. Liu, and I. A. Bilenko, Recent advances in laser self-injection locking to high-Q microresonators, *Frontiers of Physics* **18**, 21305 (2023).
 - [26] A. Dutt, K. Luke, S. Manipatruni, A. L. Gaeta, P. Nussenzveig, and M. Lipson, On-chip optical squeezing, *Phys. Rev. Appl.* **3**, 044005 (2015).
 - [27] K. Guo, L. Yang, X. Shi, X. Liu, Y. Cao, J. Zhang, X. Wang, J. Yang, H. Ou, and Y. Zhao, Nonclassical optical bistability and resonance-locked regime of photon-pair sources using silicon microring resonator, *Phys. Rev. Appl.* **11**, 034007 (2019).
 - [28] V. D. Vaidya, B. Morrison, L. G. Helt, R. Shahrokhshahi, D. H. Mahler, M. J. Collins, K. Tan, J. Lavoie, A. Reppington, M. Menotti, N. Quesada, R. C. Pooser, A. E. Lita, T. Gerrits, S. W. Nam, and Z. Vernon, Broadband quadrature-squeezed vacuum and nonclassical photon number correlations from a nanophotonic device, *Science Advances* **6**, eaba9186 (2020).
 - [29] Y. Okawachi, M. Yu, K. Luke, D. O. Carvalho, M. Lipson, and A. L. Gaeta, Quantum random number generator using a microresonator-based Kerr oscillator, *Opt. Lett.* **41**, 4194 (2016).
 - [30] A. Marandi, N. C. Leindecker, K. L. Vodopyanov, and R. L. Byer, All-optical quantum random bit generation from intrinsically binary phase of parametric oscillators, *Opt. Express* **20**, 19322 (2012).
 - [31] Z. Wang, A. Marandi, K. Wen, R. L. Byer, and Y. Yamamoto, Coherent Ising machine based on degenerate optical parametric oscillators, *Phys. Rev. A* **88**, 063853 (2013).
 - [32] T. Inagaki, K. Inaba, R. Hamerly, K. Inoue, Y. Yamamoto, and H. Takesue, Large-scale Ising spin network based on degenerate optical parametric oscillators, *Nature Photonics* **10**, 415 (2016).
 - [33] A. Marandi, Z. Wang, K. Takata, R. Byer, and Y. Yamamoto, Network of time-multiplexed optical parametric oscillators as a coherent Ising machine, *Nature Photonics* **8**, 937 (2014).
 - [34] Y. Yamamoto, K. Aihara, T. Leleu, K.-i. Kawarabayashi, S. Kako, M. Fejer, K. Inoue, and H. Takesue, Coherent Ising machines—optical neural networks operating at the quantum limit, *npj Quantum Information* **3**, 1 (2017).
 - [35] Z. Vernon, N. Quesada, M. Liscidini, B. Morrison, M. Menotti, K. Tan, and J. Sipe, Scalable squeezed-light source for continuous-variable quantum sampling, *Phys. Rev. Appl.* **12**, 064024 (2019).
 - [36] A. W. Bruch, X. Liu, J. B. Surya, C.-L. Zou, and H. X. Tang, On-chip $\chi(2)$ microring optical parametric oscillator, *Optica* **6**, 1361 (2019).
 - [37] Y. Okawachi, M. Yu, J. K. Jang, X. Ji, Y. Zhao, B. Y. Kim, M. Lipson, and A. L. Gaeta, Demonstration of chip-based coupled degenerate optical parametric oscillators

- for realizing a nanophotonic spin-glass, *Nature Communications* **11**, 4119 (2020).
- [38] T. Hansson and S. Wabnitz, Bichromatically pumped microresonator frequency combs, *Phys. Rev. A* **90**, 013811 (2014).
- [39] Y. Okawachi, M. Yu, K. Luke, D. O. Carvalho, S. Ramelow, A. Farsi, M. Lipson, and A. L. Gaeta, Dual-pumped degenerate Kerr oscillator in a silicon nitride microresonator, *Opt. Lett.* **40**, 5267 (2015).
- [40] N. Tezak, T. Van Vaerenbergh, J. S. Pelc, G. J. Mendoza, D. Kielpinski, H. Mabuchi, and R. G. Beausoleil, Integrated coherent Ising machines based on self-phase modulation in microring resonators, *IEEE Journal of Selected Topics in Quantum Electronics* **26**, 1 (2020).
- [41] N. Mohseni, P. L. McMahon, and T. Byrnes, Ising machines as hardware solvers of combinatorial optimization problems, *Nature Reviews Physics* **4**, 363 (2022).
- [42] Z. Li, R. Gan, Z. Chen, Z. Deng, R. Gao, K. Chen, C. Guo, Y. Zhang, L. Liu, S. Yu, and J. Liu, Scalable on-chip optoelectronic Ising machine utilizing thin-film lithium niobate photonics, *ACS Photonics* **11**, 1703 (2024).
- [43] Y. Zhao, Y. Okawachi, J. K. Jang, X. Ji, M. Lipson, and A. L. Gaeta, Near-degenerate quadrature-squeezed vacuum generation on a silicon-nitride chip, *Phys. Rev. Lett.* **124**, 193601 (2020).
- [44] S. Fujii, Y. Okabe, R. Suzuki, T. Kato, A. Hori, Y. Honda, and T. Tanabe, Analysis of mode coupling assisted Kerr comb generation in normal dispersion system, *IEEE Photonics Journal* **10**, 1 (2018).
- [45] S.-P. Yu, D. C. Cole, H. Jung, G. T. Moille, K. Srinivasan, and S. B. Papp, Spontaneous pulse formation in edgeless photonic crystal resonators, *Nature Photonics* **15**, 461 (2021).
- [46] J. A. Black, G. Brodnik, H. Liu, S.-P. Yu, D. R. Carlson, J. Zang, T. C. Briles, and S. B. Papp, Optical-parametric oscillation in photonic-crystal ring resonators, *Optica* **9**, 1183 (2022).
- [47] H. Seifoory, Z. Vernon, D. H. Mahler, M. Menotti, Y. Zhang, and J. E. Sipe, Degenerate squeezing in a dual-pumped integrated microresonator: Parasitic processes and their suppression, *Phys. Rev. A* **105**, 033524 (2022).
- [48] Ó. B. Helgason, M. Girardi, Z. Ye, F. Lei, J. Schröder, and V. Torres-Company, Surpassing the nonlinear conversion efficiency of soliton microcombs, *Nature Photonics* **17**, 992 (2023).
- [49] A. E. Ulanov, B. Ruhnke, T. Wildi, and T. Herr, Quadrature squeezing in a nanophotonic microresonator, *arXiv:2502.17337*.
- [50] M. H. P. Pfeiffer, A. Kordts, V. Brasch, M. Zervas, M. Geiselmann, J. D. Jost, and T. J. Kippenberg, Photonic damascene process for integrated high-Q microresonator based nonlinear photonics, *Optica* **3**, 20 (2016).
- [51] M. H. P. Pfeiffer, C. Herkommer, J. Liu, T. Morais, M. Zervas, M. Geiselmann, and T. J. Kippenberg, Photonic damascene process for low-loss, high-confinement silicon nitride waveguides, *IEEE Journal of Selected Topics in Quantum Electronics* **24**, 1 (2018).
- [52] M. H. P. Pfeiffer, J. Liu, A. S. Raja, T. Morais, B. Ghadani, and T. J. Kippenberg, Ultra-smooth silicon nitride waveguides based on the damascene reflow process: fabrication and loss origins, *Optica* **5**, 884 (2018).
- [53] M. H. Anderson, W. Weng, G. Lihachev, A. Tikan, J. Liu, and T. J. Kippenberg, Zero dispersion Kerr solitons in optical microresonators, *Nature Communications* **13**, 4764 (2022).
- [54] X. Xue, X. Zheng, and B. Zhou, Super-efficient temporal solitons in mutually coupled optical cavities, *Nat. Photonics* **13**, 616–622 (2020).
- [55] Ó. B. Helgason, F. R. Arteaga-Sierra, Z. Ye, K. Twayana, P. A. Andrekson, M. Karlsson, J. Schröder, and V. Torres-Company, Dissipative solitons in photonic molecules, *Nature Photonics* **15**, 305 (2021).
- [56] X. Lu, S. Rogers, W. C. Jiang, and Q. Lin, Selective engineering of cavity resonance for frequency matching in optical parametric processes, *Applied Physics Letters* **105**, 151104 (2014).
- [57] S. Fujii and T. Tanabe, Dispersion engineering and measurement of whispering gallery mode microresonator for Kerr frequency comb generation, *Nanophotonics* **9**, 1087 (2020).
- [58] G. Moille, X. Lu, J. Stone, D. Westly, and K. Srinivasan, Fourier synthesis dispersion engineering of photonic crystal microrings for broadband frequency combs, *Communications Physics* **6**, 144 (2023).
- [59] E. Lucas, S.-P. Yu, T. C. Briles, D. R. Carlson, and S. B. Papp, Tailoring microcombs with inverse-designed, meta-dispersion microresonators, *Nature Photonics* **17**, 943 (2023).
- [60] S.-P. Yu, E. Lucas, J. Zang, and S. B. Papp, A continuum of bright and dark-pulse states in a photonic-crystal resonator, *Nature Communications* **13**, 3134 (2022).
- [61] X. Lu, A. McClung, and K. Srinivasan, High-Q slow light and its localization in a photonic crystal microring, *Nature Photonics* **16**, 66 (2022).
- [62] K. Y. Yang, C. Shirkurkar, A. D. White, J. Zang, L. Chang, F. Ashtiani, M. A. Guidry, D. M. Lukin, S. V. Pericherla, J. Yang, H. Kwon, J. Lu, G. H. Ahn, K. Van Gasse, Y. Jin, S.-P. Yu, T. C. Briles, J. R. Stone, D. R. Carlson, H. Song, K. Zou, H. Zhou, K. Pang, H. Hao, L. Trask, M. Li, A. Netherton, L. Rechtman, J. S. Stone, J. L. Skarda, L. Su, D. Vercruysse, J.-P. W. MacLean, S. Aghaeimeibodi, M.-J. Li, D. A. B. Miller, D. M. Marom, A. E. Willner, J. E. Bowers, S. B. Papp, P. J. Delfyett, F. Aflatouni, and J. Vučković, Multi-dimensional data transmission using inverse-designed silicon photonics and microcombs, *Nature Communications* **13**, 7862 (2022).
- [63] V. E. Lobanov, O. V. Borovkova, A. K. Vorobyev, D. M. Sokol, N. Y. Dmitriev, A. E. Shitikov, D. A. Chermoshentsev, and I. A. Bilenko, Generation of triangular pulse trains in normal-dispersion photonic crystal microresonators, *Phys. Rev. A* **110**, 063526 (2024).
- [64] X. Lu, A. Chanana, Y. Sun, A. McClung, M. Davanco, and K. Srinivasan, Band flipping and bandgap closing in a photonic crystal ring and its applications, *Opt. Express* **32**, 20360 (2024).
- [65] G. Spektor, J. Zang, A. Dan, T. C. Briles, G. M. Brodnik, H. Liu, J. A. Black, D. R. Carlson, and S. B. Papp, Photonic bandgap microcombs at 1064 nm, *APL Photonics* **9**, 021303 (2024).
- [66] A. E. Ulanov, T. Wildi, N. G. Pavlov, J. D. Jost, M. Karpov, and T. Herr, Synthetic reflection self-injection-locked microcombs, *Nature Photonics* **18**, 294 (2024).
- [67] J. Zang, S.-P. Yu, H. Liu, Y. Jin, T. C. Briles, D. R. Carlson, and S. B. Papp, Laser-power consumption of soliton formation in a bidirectional Kerr resonator, *arXiv:2401.16740*.

- [68] Y. K. Chembo and N. Yu, Modal expansion approach to optical-frequency-comb generation with monolithic whispering-gallery-mode resonators, *Phys. Rev. A* **82**, 033801 (2010).
- [69] J. R. Stone, G. Moille, X. Lu, and K. Srinivasan, Conversion efficiency in Kerr-microresonator optical parametric oscillators: From three modes to many modes, *Phys. Rev. Appl.* **17**, 024038 (2022).
- [70] T. Hansson, D. Modotto, and S. Wabnitz, On the numerical simulation of Kerr frequency combs using coupled mode equations, *Optics Communications* **312**, 134 (2014).
- [71] X. Xue, Y. Xuan, Y. Liu, P.-H. Wang, S. Chen, J. Wang, D. E. Leaird, M. Qi, and A. M. Weiner, Mode-locked dark pulse Kerr combs in normal-dispersion microresonators, *Nature Photonics* **9**, 594 (2015).
- [72] V. E. Lobanov, A. E. Shitikov, R. R. Galiev, K. N. Min'kov, and N. M. Kondratiev, Generation and properties of dissipative Kerr solitons and platicons in optical microresonators with backscattering, *Opt. Express* **28**, 36544 (2020).
- [73] Z.-R. Yang and P.-H. Wang, Stability analysis of mode-coupling-assisted microcombs in normal dispersion, *Opt. Express* **30**, 37637 (2022).
- [74] V. E. Lobanov, N. M. Kondratiev, A. E. Shitikov, O. V. Borovkova, S. J. Cordette, and I. A. Bilenko, Platicon stability in hot cavities, *Opt. Lett.* **48**, 2353 (2023).
- [75] J. K. Jang, Y. Okawachi, M. Yu, K. Luke, X. Ji, M. Lipson, and A. L. Gaeta, Dynamics of mode-coupling-induced microresonator frequency combs in normal dispersion, *Opt. Express* **24**, 28794 (2016).
- [76] Y. Zhang, M. Menotti, K. Tan, V. D. Vaidya, D. H. Mahler, L. G. Helt, L. Zatti, M. Liscidini, B. Morrison, and Z. Vernon, Squeezed light from a nanophotonic molecule, *Nature Communications* **12**, 2233 (2021).
- [77] Y. Jin, E. Lucas, J. Zang, T. Briles, I. Dickson, D. Carlson, and S. B. Papp, The bandgap-detuned excitation regime in photonic-crystal resonators, arXiv:2404.11733.